A model study of tropical gravity wave changes with El Niño and La Niña conditions and wave forcing of the quasibiennial oscillation

M. Joan Alexander*

NorthWest Research Assoc.–CoRA Office, Boulder, CO

David A. Ortland

NorthWest Research Assoc.–Seattle Office, Redmond, WA, USA

Alison W. Grimsdell

NorthWest Research Assoc.–CoRA Office, Boulder, CO

Jie-Eun Kim

University of Washington/JISAO

**Corresponding author address:* NorthWest Research Associates–CoRA Office, 3380 Mitchell Lane, Boulder, CO 80301

E-mail: alexand@nwra.com

ABSTRACT

Using an idealized model framework with high-frequency tropical latent heating variability derived from global satellite observations of precipitation and clouds, we examine the properties and effects of gravity waves in the lower stratosphere, contrasting conditions in an El Niño and La Niña year. The model generates a broad spectrum of tropical waves including planetary-scale waves through mesoscale gravity waves. We compare modeled monthly-mean regional variations in wind and temperature with reanalyses, and we validate the modeled gravity waves using satellite- and balloon-based estimates of gravity wave momentum flux. Some interesting El Niño Southern Oscillation (ENSO) changes in the gravity spectrum of momentum flux are found in the model which are discussed in terms of the ENSO variations in clouds, precipitation, and large-scale winds. The modeled intermittency in gravity wave momentum flux is shown to be very realistic compared to observations, and the largest amplitude waves are related to significant gravity wave drag forces in the lowermost stratosphere. This strong intermittency is generally absent or weak in climate models due to deficiencies in parameterizations of gravity wave intermittency. Our results suggest a way forward to improve model representations of lowermost stratospheric quasi-biennial oscillation winds and teleconnections.

1. Introduction

Long-range weather forecast skill has demonstrated links to the tropical stratosphere. The quasi-biennial oscillation (QBO), a reversal of the tropical lower stratosphere zonal mean winds roughly every other year, is an important source of predictability for seasonal forecasts of the North Atlantic Oscillation (NAO) [Scaife et al. 2014a]. Although confined to tropical latitudes, the QBO has clear connections to polar stratospheric extreme vortex events [Holton and Tan 1980] and extratropical surface weather conditions [Thompson et al. 2002; Garfinkel et al. 2012]. The QBO also modulates the chemical composition of the stratosphere, for example dominating interannual variability in tropical stratospheric water vapor with associated effects on chemistry and temperature [Mote et al. 1996; Randel et al. 2004].

The key characteristics of the QBO are zonal mean winds that oscillate from easterly to westerly with an average period of 28 months and ranging from $\sim$22 to 34 months. The circulation is not locked to the annual cycle, rather the period is inversely related to atmospheric wave momentum transport, or more specifically to the divergence of Eliassen-Palm flux [Dunkerton 1997], which is often called wave drag or wave forcing. A range of studies have identified tropical gravity waves as a crucial component of the momentum transport necessary to drive the QBO, with current estimates suggesting more than half of the flux is carried by gravity waves that are generated by tropical convection (e.g. Kawatani et al. [2010a]). Global characterizations of gravity waves and their momentum transport remain an observational challenge due to their small scales, high frequencies, and intermittent occurrences [Geller et al. 2013; Alexander 2015]. Models therefore play a major role in our understanding of tropical gravity waves and their effects on circulation.

Despite the fact that the basic wave-mean flow interaction mechanism that forces the QBO has been understood for decades, most climate models still do not have a QBO. The global climate and weather forecasting models that do include a QBO rely on parameterization of sub-grid-scale gravity wave forcing. Such parameterizations often assume an average set of wave properties, continually forced at all times and all longitudes. A few climate models include varying gravity wave properties that are tied to the model's parameterized convection (e.g. Richter et al. [2014], Bushell et al. [2015]), but large uncertainties in specifying the properties of the sub-gridscale gravity waves remain [Schirber et al. 2015].

In this study, we employ a global model that is uniquely constrained by observations in multiple ways in order to examine interannual, subseasonal, and geographical variability in tropical gravity waves and their effects on the stratospheric circulation. The model is designed to represent the scales of gravity waves that are observed by limb-sounding satellite measurements, which provide constraints for the modeled gravity wave momentum transport. Global precipitation and cloud observations provide constraints on variability in latent heating that force the waves in the model. Finally, zonal mean winds in the model are relaxed to those in reanalysis, and the model is initialized with reanalyzed zonal mean temperaturess in order to realistically constrain wave propagation and interactions with the circulation.

In section 2, we describe the precipitation and cloud data that will be used to estimate latent heating that forces tropical waves in the model. Section 3 describes the model experiment design, the latent heating algorithm, and the properties of tropical clouds, precipitation, and latent heating for the two experiments in El Niño and La Niña conditions. Section 4 describes the model results and compares them to observations, including tropical tropopause wind and temperature variations, the properties of the gravity waves, and wave driving of the QBO. Section 5 is a discussion of the results and their implications for global climate and weather modeling, and section 6 is a summary with conclusions.

2. Data Description

a. Background

The launch of the Tropical Rainfall Measuring Mission (TRMM) satellite in 1998 began an era of high-resolution global precipitation measurement. TRMM products include the TMPA (3B42) gridded rain rates at $0.25° \times 0.25°$ spatial resolution and 3-hourly time intervals [Huffman et al. 2007]. Ryu et al. [2011] described an algorithm for computing the 3-dimensional time-dependent latent heating field using TRMM 3B42 rain rates, and ancillary cloud-top height derived from global merged geostationary satellite observations of infrared brightness temperatures. The resulting three-dimensional time-dependent latent heating field defined sources for waves with periods longer than 6 hours in a dry dynamical primitive equation model. Ortland et al. [2011] used this method to study the sensitivity of the wave Eliassen-Palm flux (EP-flux) spectrum to spatial resolution in the model. They showed that at the 3-hourly temporal resolution of the TRMM 3B42 data, spatial resolutions resolving wavenumbers higher than 60 gave only minor increases in the EP-flux. Thus for modeling gravity waves, the 3-hourly time resolution was clearly a limiting factor. Higher-frequency gridded precipitation products available include CMORPH [Joyce et al. 2004] with 8-km spatial and 30-min temporal resolution, GSMAP with $0.1°$ spatial and 1-hourly temporal resolution [Ushio et al. 2009], and a recent product called IMERG [Huffman et al. 2015, ATBD] with $0.1°$ spatial and 30-min temporal resolution based on new measurements from the Global Precipitation Missions (GPM). IMERG is currently only available beginning in 2014, although there are plans to extend the IMERG record back in time. For the present study, we seek to model the historical period 2006-2007, a time when we have high-resolution satellite limb-sounding observations that we can use for validation of gravity wave momentum fluxes [Alexander 2015]. We therefore utilize CMORPH rain rates degraded to $0.25° \times 0.25°$ spatial resolution but utilizing the full 30-min temporal resolution. The focus in this work will be on tropical convective wave sources within $\pm 30^\circ$ of the equator.

b. CMORPH Precipitation

Like other high-resolution precipitation products, CMORPH takes advantage of the frequent sampling of geostationary infrared measurements and combines these with higher-quality microwave precipitation measurements to create a gridded spatio-temporally varying precipitation rate product. Sapiano and Arkin [2009] found 3-hourly CMORPH $0.25^\circ \times 0.25^\circ$ data showed the highest correlations against gauge data among several comparable data sets. However, all showed a tendency to underestimate rainfall over the tropical Pacific Ocean. Habib et al. [2012] evaluated CMORPH at 8 km $\times$ 8 km, 30-min resolution against dense rain gauge observations and radar-based estimates in Louisiana. CMORPH was found to have negligible bias over the 28-day study period, high detection skills and rainfall occurrence distributions that compare very well to the radar. Significant biases occurred on event scales, and missed and false-rain detections were $\sim$20%, but these errors are reduced considerably through aggregation. Our degradation to $0.25^\circ \times 0.25^\circ$ resolution partly serves that purpose, and we will further focus on statistics of wave generation with a full month of data.

c. Global-merged Infrared Brightness Temperature and Cloud-top Height

TRMM ancilliary data include global merged infrared brightness temperatures utilizing the international set of geostationary measurements. The merged data is available equatorward of 60° at 4-km spatial resolution and 30-min time resolution. As for the rain rate data, we degrade these brightness temperatures to $0.25^\circ \times 0.25^\circ$ spatial resolution but retain the 30-min temporal resolution. Occasional gaps in coverage occur but are filled by linear interpolation in time utilizing measurements in the previous and following 1.5 hours to achieve a continuous coverage. A small but persistent gap in coverage occurs in the tropical Southern Hemisphere eastern Pacific, but since this is a generally dry region, it is unlikely to affect our results. Cloud-top height is estimated by matching the observed brightness temperature to regional temperature profiles taken from the MERRA reanalysis [Rienecker et al. 2011].

Figure 1 shows sample snapshots of the resulting rain rates and cloud-top heights at $0.25^{\circ}\times0.25^{\circ}$, 30-min resolution.

3. Experiment Design

a. Latent heating

Using the precipitation rates and cloud top heights from section 2, a three-dimensional, time-dependent tropical latent heating field is calculated with the algorithm described in detail in Ryu et al. [2011]. Briefly summarizing the procedure, a combined rain-rate and cloud-height criterion categorizes the heating profile as convective or stratiform type. For the convective-type rain, heating is specified as positive everywhere with a half-sine vertical profile shape, and heating depth and peak heating are functions of rain-rate and cloud top height. For stratiform-type rain, melting level is a function of rain rate, and peak upper tropospheric heating rate and peak lower tropospheric cooling rate are functions of rain-rate and cloud height. The algorithm is similar to the TRMM Spectral Latent Heating (SLH) product [Shige et al. 2007]. In particular, it includes a factor that accounts for horizontal transport of precipitation from convective to stratiform regions.

This three-dimensional latent heating is computed at the same 30-min resolution as the cloud and precipitation data. The latent heating field can be compared to other existing latent heating products after sufficient averaging. The appendix provides some additional information about the latent heating.

b. Model

A global nonlinear spectral model is used to simulate waves forced by the space-time-varying tropical latent heating. The model was described previously in Ortland et al. [2011]. In the present cases, the model is initialized with November monthly mean zonal winds and temperatures and run for two months, through the end of December. We subsequently analyze the December results only. The model troposphere is forced with the three-dimensional, time-varying latent heating field, which forces a broad spectrum of waves, including global-scale equatorial Rossby and Kelvin waves through mesoscale gravity waves. Newtonian cooling is applied to the perturbation temperature, where a perturbation is defined as the deviation from the daily MERRA zonal mean. The time scale of the Newtonian cooling is 5 days in the stratosphere and 25 days in the middle and upper troposphere [Ryu et al. 2011]. In the lower troposphere below 650 hPa (σ >0.7), the Newtonian cooling time scale gradually decreases to 8 days at the lowest model level [Held and Suarez 1994]. The zonal-mean zonal wind is relaxed to a time-varying state defined by the daily zonal-mean MERRA zonal wind at a rate of .05 d^{-1} to ensure realistic QBO shear throughout the simulation. The vertical grid consists of 130 sigma levels with a uniform resolution of 500 m between the surface and 65 km. The top ~30 km of the model serves as a sponge layer where wind perturbations are strongly damped with Rayleigh friction. The friction starts from zero at 30 km and ramps with with a tanh function shape to a maximum of 7 d^{-1} above 45 km. An eighth-order horizontal hyper-diffusion is used to prevent energy from accumulating at the smallest model scales. It is set to damp the smallest scale at a rate of 1 d^{-1}. The horizontal resolution is truncated at T120, resulting in a resolution of ~150km, a scale chosen to permit simulation of gravity waves resolved in limb-sounding satellite observations [Alexander 2015] that we will use to validate the modeled gravity waves. We force the model with the zonally-symmetric component of the heating removed, and focus on analysis of waves with periods shorter than 30 days.

c. Experiments

We simulate two December periods in 2006 and 2007. These represent, respectively, weak El Niño and strong La Niña events as seen in the time series of the ENSO 3.4 index shown in Figure 2. Following the characteristic pattern for such conditions, precipitation in the December 2006 period was strongest in the central and eastern Pacific, while the precipitation maximum shifted to the Indian Ocean/Maritime Continent region in December 2007. Both Decembers also included significant precipitation variability associated with the Madden-Julian Oscillation (MJO), also shown in Fig. 2. The MJO is only active during the last 13 days of December 2006, while it is active throughout December 2007. For 2006, the MJO activity is focused in the eastern Indian Ocean and Maritime Continent (phases 3-4), whereas in 2007 the signal propagates from Africa to the Maritime Continent (phases 1-4).

The properties of waves forced by convective heating are sensitive to both the strength of the heating and the depth of the heating (e.g. Salby and Garcia [1987]; Bergman and Salby [1994]; Holton et al. [2002]; Beres [2004]). Geller et al. [2016] suggest that changes in these parameters with ENSO may explain previously observed sensitivity of the QBO to ENSO conditions. Thus to help place our wave analysis results presented later in context, we compare here occurrence frequency distributions of rain rate and cloud-top height for our two cases.

Figure 3 compares distributions of tropical rain rates and cloud top heights for December 2006 and December 2007 at latitudes most relevant to the QBO (10°S-10°N). These distributions represent "convective" pixels only, defined as those with rain rates greater than 1.6 mm hr^{-1}. The two distributions are very similar, with no significant differences in the mean values. The La Niña year (2007) displays slightly more of the deepest clouds and higher rain rates, however there are fewer convective pixels overall, only 3.5% in December 2007 compared to 4.3% in December 2006. While ENSO dramatically affects the geographical patterns in precipitation, Fig. 3 suggests that globally these statistics of tropical convective rain rate and cloud depth remain relatively constant.

4. Results

a. Monthly-mean Patterns in Latent Heating and Tropopause Wind and Temperature

Figure 4 shows the December mean heating rates at the 400 hPa level at $0.25° \times 0.25°$ resolution. Characteristic patterns associated with El Niño (2006) and La Niña (2007) are clearly visible in these panels. Note that rates in Fig. 4 are shown at finer horizontal resolution than the model. To force the model, 30-min heating rates are spectrally decomposed with spatial spherical harmonics and truncated to T120 ($\sim 1.5°$ resolution), and the 30-min rates are linearly interpolated in time to the model 3-min timestep.

Figure 5 compares December-mean tropopause (~17 km) temperature maps for the MERRA reanalysis and the model. The deepest latent heating in the model extends only to the 15-km level, so these maps represent the dynamical responses to latent heating above those levels that are directly forced. Note that the model initial conditions are zonally symmetric, so the longitudinal variations in temperature result solely from wave responses to the tropospheric heating. The top panels compare December 2006, and December 2007 is compared in the bottom panels. The same comparison of monthly-mean zonal winds is shown in Figure 6. In these model monthly-means, we are primarily seeing the projections of the slowly varying equatorial Rossby and Kelvin wave modes on the tropopause temperature and wind structure. The stronger asymmetry in rain and heating across the equator in the 2006 El Niño period leads to stronger responses in the equatorial Rossby waves and characteristic off-equator temperature minima. Conversely in 2007, the western Pacific temperature minimum and zonal winds are stronger on the equator and likely also related to the stronger MJO activity there and stronger Kelvin wave responses. Similar tropopause responses to latent heating variations were reported in the idealized model study of Norton [2006].

While the model shows differences from MERRA in these monthly-mean comparisons, the degree to which our highly idealized model does capture the observed zonally-asymmetric wind and temperature pattern differences in these two years is due to the realism of the monthly-mean heating distribution that is forcing the model. The comparison highlights the importance of waves forced by tropical latent heating in controlling the upper-level circulation and temperature structure.

b. Gravity Wave Spectrum

With heating varying on a 30-min timescale, the response in the model includes a broad spectrum of gravity waves. We seek to identify relationships between the gravity waves generated by the different latent heating variations, as well as their effects on the circulation in the lower stratosphere. The differences in the zonal mean winds in December 2006 and December 2007 are strong at QBO altitudes, beginning at 18 km and above (Fig. 2c). The QBO wind variations will dramatically alter the spectrum of waves through wave-mean flow interaction. We therefore begin here by examining the vertical flux of horizontal momentum, which describes the gravity wave contribution to the EP-flux [Andrews et al. 1987], and we examine this at the tropopause ($\sim$17 km), which is above the direct latent heating forcing but below the QBO wind influences on the spectrum. This permits an examination of the influences on the tropospheric latent heating and circulation on the vertically propagating wave spectrum in isolation from stratospheric wave-mean flow interactions.

We perform 3-dimensional spectral analysis as a function of longitude, latitude, and time on overlapping 50° longitudinal sectors spanning latitudes ±25° over 3-day periods. Wind anomalies in the zonal and meridional directions (u', v') are computed as deviations from the $50° \times 50°$ sector trends, and cosine taper functions in latitude and longitude are applied. The longitude sectors overlap by 5° on each side where the taper=1/2 such that the total flux in all sector spectra equals the global total, and each spectrum after tapering represents a $\sim 40° \times 40°$ region. The effective horizontal wavelength range resolved in the spectrum is 227-4447 km. Complex 3-dimensional transforms $(\hat{U}, \hat{V})$ are then multiplied by the complex conjugate of the vertical wind transform $\hat{W}^*$ computed on the same grid, and the real part multiplied by atmospheric density gives the spectral density of vertical flux of horizontal momentum

$$F_M = \rho[\mathrm{Re}(\hat{U}\hat{W}^*), \mathrm{Re}(\hat{V}\hat{W}^*)]/\Delta k_x/\Delta k_y/\Delta\omega,$$

where (k_x, k_y) is the horizontal wavenumber vector and ω the frequency. The results are rebinned in terms of azimuthal direction of propagation (° from east) and phase speed (c) and renormalized to spectral density in these coordinates. Results for Dec 2006 and 2007 are shown in Figure 7, where we have further reduced the maximum wavelength included in these spectra to wavenumbers>12 (3335 km). The spectra have been averaged over 15-17 km (above the direct latent heating forcing and below the QBO) to best represent the gravity waves entering the stratosphere prior to their interaction with the QBO winds.

The spectra show some clear differences, but mainly similarities. 2006 shows a weak preference for westward propagation compared to eastward, while 2007 shows a strong peak in the east-northeast direction and relatively weak westward flux. Meridional fluxes are more similar in the two years. At higher phase speeds, $c > 20$ m s^{-1} the spectra are very similar, displaying a much broader westward spectrum and narrower eastward spectrum. To bring out phase speeds relevant to the QBO, Figure 8 shows the phase speed spectrum of the zonal flux only. The La Niña case (2007) has larger flux overall, while the El Niño case shows slightly larger fluxes over a narrow range near $c = -20$ m s^{-1}. Note, however, that we do not examine north-south asymmetries in gravity waves, which have shown sensitivity to ENSO in previous work [Sato et al. 2016].

Figures 9 and 10 examine regional variations in the spectrum. Not surprisingly, these are substantial, and the fluxes vary to some degree with regional variations in the heating. Clearly the ENSO variations in heating give rise to strong regional variations in the gravity wave spectra although the zonal mean spectra (Figs. 7 and 8) were relatively more similar. Surprisingly, the strong El Niño heating in the Dec 2006 central Pacific does not result in much stronger gravity wave momentum fluxes. The reason is likely related to different tropopause winds (Fig. 9c): Tsuchiya et al. [2016] found stronger tropical gravity wave activity correlated with westward tropopause winds, while in the central and eastern Pacific those winds are eastward. Note that the spectra over the Indian Ocean and S. America show secondary peaks in westward propagating waves at the slowest phase speeds. This is a spectral signature of the obstacle effect for wave generation associated with the upper troposphere westward winds interacting with deep convection [Alexander et al. 2006]. If these waves were instead generated in the middle troposphere, they would have been filtered by the upper troposphere westward winds. These regional spectra also make it clear that the strongest east/west asymmetries occur over these regions plus the African and S. American tropics, where we see much faster westward phase speeds and much stronger eastward fluxes at $c < 10$ m s^{-1}.

Figs. 9c and 10c summarize the geographical and interannual variations in tropopause gravity wave momentum flux more quantitatively. Each symbol represents absolute momentum flux in a $40^\circ \times 40^\circ$ region, $\pm 20^\circ$ latitude straddling the equator. In both of our simulated years, the Indian

Ocean and Maritime Continent regions are the locus of strongest tropopause gravity waves, where tropopause winds are also westward. The strongest fluxes in our simulations occur in December 2007 in the sector surrounding Sumatra, a locus of MJO activity throughout an extended portion of the month (Fig. 2), suggesting that MJO precipitation variability might have greater effect on gravity wave momentum fluxes than ENSO variability. Note that while a strong peak in total omni-directional flux occurs in the central Pacific in the 2006 El Niño year, the peak in total zonal flux is muted due to strong filtering of eastward propagating waves in this region of eastward tropopause winds. In the 2007 La Niña year we see a peak in the Sumatra sector in total omni-directional flux as well as a strong peak in zonal flux, which is associated with the peak in eastward waves (Fig. 9b) propagating through westward tropopause winds.

c. Validation of modeled momentum fluxes

Recent research has highlighted the high degree of intermittency in the occurrence of gravity waves with different amplitudes [Hertzog et al. 2008; 2012; Jewtoukoff et al. 2013; Plougonven et al. 2013; Alexander and Grimsdell 2013; Alexander 2015; Wright et al. 2013]. Observations display log-normal distributions of gravity wave momentum fluxes with infrequent but large events that contain much of the total flux. This high degree of intermittency can be quite important to gravity wave effects on circulation [de la Cámara et al. 2014; Bushell et al. 2015]. Specifically, the larger amplitude waves in the tails of the distributions can break at lower altitudes and result in larger forcing in the stratosphere. Here we examine mean gravity wave momentum fluxes as well as momentum flux frequency distributions in the model, and we compare both to observations.

Zonal and meridional wind anomalies are computed as in section 4.2 and the products of horizontal and vertical anomalies and density $\frac{1}{2}\rho((u'w')^2 + (v'w')^2)^{1/2}$ give an estimate of the local momentum flux magnitudes. This method gives accurate maximum values if waves are intermittent such that packets appear in relative isolation, an assumption relevant to the lower stratosphere. Ideally, the wind covariances would be averaged over a period or wavelength, however we use this approximate method following previous work [Plougonven et al. 2013].

Figure 11a shows occurrence frequencies of these gravity wave momentum fluxes at 20 km, contrasting Dec 2006 (red) and 2007 (blue), and observations from limb-sounding satellites [Alexander 2015] ("HIRDLS/COSMIC", black). The number of measurements in the satellite retrievals in a single month is too small to fill a distribution, so we use 13 month totals Dec 2006-Dec 2007 for comparison to the model results in Fig. 11a. Means of the distributions are 5.2 mPa for the Dec 2006 model, and 5.8 mPa for the Dec 2007 model. Averaging the available observations we obtain a mean of 3.2 mPa in Dec 2006 (522 measurements) and 3.9 mPa in Dec 2007 (323 measurements). Note that to determine momentum flux from the observations required a wavelet analysis of the vertical structure, so it is not truly a measurement at a single level, but it combines wave amplitude information over a range of altitudes that varies with the wave vertical wavelength. Dec 2007 fluxes are larger than Dec 2006 in both the observations and the model.

Pre-Concordiasi long-duration balloon measurements covered all longitudes at an altitude near 20 km [Jewtoukoff et al. 2013]. The Pre-Concordiasi campaign occurred during a 3 month period February-May, 2010, and the campaign average momentum fluxes from the two tropical balloons were reported at 3.9 and 5.4 mPa. The Pre-Concordiasi values include the spectrum of gravity waves from the buoyancy period to 1-day period, while our model cannot represent waves with periods shorter than 1 hour due to the 30-min resolution of the forcing but includes periods up to 3 days. Thus neither the satellite nor the balloon observational comparisons can be considered exact, but these comparisons do suggest the modeled fluxes are reasonably similar to the observations.

All of these momentum flux distributions approximately represent log-normal, non-Gaussian distributions. The standard deviation is therefore large compared to the mean value, but this does not indicate a lack of significance. Jewtoukoff et al. [2013] considered the difference between the two Pre-Concordiasi balloons as significant and attributed the difference to geographic sampling: The second balloon with larger mean flux spent more time above the Indian Ocean/West Pacific Ocean sectors where the occurrence of multicellular convection was concentrated and where we also see largest momentum fluxes. Similarly, it is likely that the differences between the model in Dec 2006 and Dec 2007 are also significant given the distinct peaks in the fluxes seen in the spectrum (Fig. 7). However, the uncertainties in the heating derived from CMORPH precipitation would also need to be considered in order to claim a statistically significant difference between the two cases. Both the 3D satellite observations and the model suggest somewhat larger fluxes in Dec 2007 than in Dec 2006.

At 20 km, QBO wind shears will have filtered some of the gravity waves. To isolate differences associated with the tropical tropospheric conditions in the two years, we also show modeled momentum flux distributions at the tropopause ($\sim$17 km) in Fig. 11b, an altitude just below the QBO shear zones. Note the expanded abscissa range to show the higher values that occur at this altitude. Here interannual differences appear more prominently in the extended tail of the distribution, and statistics for these distributions are shown in Table 1. The percentile statistics indicate that in Dec 2007 for example, fluxes larger than 20 mPa occur only 10% of the time (90^{th} percentile) but correspond to 54% of the total flux. This indicates that while convective waves are not quite as intermittent as orographic waves observed over Southern Hemisphere topography [Hertzog et al. 2012; de la Cámara and Lott 2015], the convective waves display a substantially larger degree of intermittency than is commonly assumed in non-orographic gravity wave parameterizations (see Bushell et al. [2015]). By comparing our mean tropopause fluxes to the 20 km values given earlier, a large fraction ($\sim$45%) of the flux has already dissipated in QBO shear zones below 20 km.

d. QBO Wave Driving

We can also examine the tropical wave EP-fluxes and flux divergences in the model. EP-flux divergence is a measure of the wave drag forces acting on the QBO. We also investigate the types of waves responsible for these forces in the model.

Figure 12 shows zonal wavenumber-frequency spectra of the absolute value of the vertical component of the EP-flux at 20 km and profiles of the divergence of this flux in Dec 2006 (a,b) and 2007 (c,d). In b and d, two profiles of each color represent separate integrations over eastward-only (positive) or westward-only (negative) wavenumbers. Black profiles represent integrals over the full halves of the spectrum. Red profiles are integrals over only the planetary-scale waves, which we define as frequencies less than 1 cyc d^{-1} and wavenumbers less than 12, illustrated with a small box near the origin in the two figures. The differences between red and black profiles then show the contributions from eastward and westward propagating gravity waves to the force on the circulation.

In 2006, gravity waves account for almost all the westward forcing, whereas in 2007 the eastward forcing is more equally proportioned between gravity waves and Kelvin waves. Note also that in both cases contributions from gravity waves are substantial even below 20km. Close examination of the two panels in Fig. 11 reveal that changes in the momentum flux distributions between 17 km and 20 km are mostly due to the loss of infrequently occurring, large amplitude waves, and similar changes with altitude have also been seen in other models [Hertzog et al. 2012]. We note that these large amplitude waves are missing in parameterizations of convective gravity wave drag (see Bushell et al. [2015]), which may explain why models tend to poorly represent the QBO in the lower stratosphere. Conversely, our model with realistic distributions in gravity wave sources (i.e. latent heating) generates a much more realistic distribution of gravity wave amplitudes, and hence significant gravity wave forces in the lowermost stratosphere.

5. Discussion

Recent work has shown clearly the very intermittent nature of gravity waves. The intermittency in our simulations (Fig. 11a) compares well to observations at an altitude near 20 km. Bushell et al. [2015] show tropical momentum flux distributions for different gravity wave parameterizations (their Fig. 6). Their invariant non-orographic parameterization dropped 4 decades in occurrence at a flux of 6 mPa. Essentially, all of the waves in the parameterization are weak in amplitude and not intermittent. They also showed the distribution of gravity wave momentum fluxes using a variable convective source parameterization. In this case, occurrences drop 4 decades at a flux of $\sim$20-25 mPa, which is much more realistically intermittent than the invariant parameterization, but the intermittency falls far short of that observed or that produced in our model. In particular, long-duration balloon observations [Jewtoukoff et al. 2013] (their Fig. 15) show that the momentum fluxes drop 4 decades in occurrence at flux values $\sim$100 mPa, and this occurs at $\sim$80 mPa in our simulations.

Typical invariant non-orographic gravity wave parameterizations have only very weak forces in the stratosphere. They are designed instead to give realistic circulation effects in the mesosphere. Orographic gravity waves are parameterized with much larger amplitudes than non-orographic waves, and as a result they break and change the circulation in the upper troposphere and lower stratosphere. However, large amplitude waves from convection do occur, and the momentum flux convergences in the stratosphere can lead to substantial forces. For example, Stephan et al. [2016] showed that realistic waves from summertime convection over the U.S. produce forces in the lower stratosphere that rival orographic wave forcing. Most parameterizations in models give relatively very small wave forces at stratospheric levels. Stochastic non-orographic parameterization methods that account for realistically intermittent amplitudes have been developed [de la Cámara and Lott 2015], and implementation in a global model showed improvements in the timing of the springtime transition from westerly to easterly winds in the Southern Hemisphere stratosphere [de la Cámara et al. 2016]. So including realistic intermittency in parameterized non-orographic gravity wave amplitudes, while simulataneously reducing gravity wave drag due to orographic waves, may be a way forward. Indeed, climate models struggle to simultaneously simulate realistic Northern and Southern Hemispheric stratospheric winds, which could be due to an over-reliance on orographic gravity wave drag.

Similarly, we find support for much larger intermittency in tropical convective gravity waves than is typically parameterized, and we hypothesize this is the reason that models struggle to represent realistic QBO winds and wind shears in the lower stratosphere at levels below 40 hPa (e.g. Krismer and Giorgetta [2014]; Richter et al. [2014]; Coy et al. [2016]). Typical gravity wave parameterizations drive only the upper levels of the QBO while planetary scale waves are responsible for most or all of the forcing at the lower levels. An early example with an invariant parameterization was shown in Giorgetta et al. [2002]. More recently Richter et al. [2014] showed modern results with a variable convective source parameterization that gave a very realistic QBO at pressure levels above 40 hPa, but in the lower stratosphere the westerly phases are too strong and easterly phases too weak. Yoo and Son [2016] have shown that easterly QBO winds in the lower stratosphere are associated with stronger tropical intraseasonal precipitation in the observational record. Hence such errors in modeled QBO winds may hinder a model's ability to represent the observed stratosphere-troposphere connections. We also note that many previous studies have suggested that the easterly QBO wind phases are forced primarily by gravity wave drag (e.g. Dunkerton [1997]; Kawatani et al. [2010a]).

More realistic intermittency such as shown in our Fig. 11 does in fact lead to significant forces in the lower stratosphere below 20 km (Fig. 12). That these forces are due to dissipation of the largest amplitude waves is also evident from comparison of the distributions at 17 km and 20 km shown in Fig. 11. Nearly half of the gravity wave momentum flux is dissipated between these levels in our model.

Our results may be relevant for realizing the long-range forecast skill that is expected from realistic representation of the tropical stratosphere in forecast models. Although the Scaife et al. [2014a] study found the QBO among the four leading sources of skill in their winter seasonal forecasts of the NAO, their forecast model's QBO teleconnection pattern was weaker than in the observations. As mentioned above, model representations of the QBO tend to be least realistic at low levels below 40 hPa, and discrepances in the width of the QBO are also common [OSullivan and Young 1992; Hansen et al. 2013]: Either or both of these could be reasons for weaker teleconnections in models. Maximum correlations between extratropical winter conditions and QBO winds have been observed with 50 hPa QBO wind in observations. If the lower levels of the QBO are unduly important to describing extratropical teleconnection strength, it points to a clear weakness in models. Further, the results of Yoo and Son [2016] suggest that long-range forecasting skill in tropical intraseasonal precipitation may be tied to realistic representation of the QBO at lower stratosphere levels in models.

While studies have shown the QBO to be highly predictable on time scales longer than a year [Scaife et al. 2014b] the unprecedented disruption of the QBO in 2016 and the failure of forecast models to predict it [Newman et al. 2016; Osprey et al. 2016] place new emphasis on more realistic representation of the wave forcing of the QBO. There is also observational evidence that the QBO winds at low levels near 70 hPa may be experiencing a long-term weakening trend [Kawatani and

Hamilton 2013]. Hence more realistic simulation of the QBO may also be beneficial to near-term climate prediction as well as seasonal forecast model skill.

In addition to forcing the stratosphere and mesosphere, gravity waves from convection can also directly force the circulation in the upper atmosphere and ionosphere [Vadas and Liu 2013; Vadas et al. 2014]. The gravity waves that can propagate to these high altitudes have fast phase speeds, faster than $\sim$50 m s^{-1}. While the peaks in our integrated phase spectra (Figs. 7-8) occurred at phase speeds $\sim$7-20 m s^{-1}, the spectra in Fig. 12 show that much faster waves also appear at higher frequencies. In These maps also make it clear that the strongest east/west asymmetries occur over these regions plus the African and S. American tropics, where we see much faster westward phase speeds and much stronger eastward fluxes at $c < 10$ m s^{-1}. particular, a lobe with phase speeds of 70 m s^{-1} among the westward propagating highest frequencies is prominent. According to the linear dispersion relation (neglecting wind effects) vertical wavelength $\lambda_Z \sim 2\pi c/N$, these fast waves would have λ_Z $\sim$44 km in the troposphere, which is close to four times the most common cloud and heating depth in our simulations of 11 km (Fig. 3). While a vertical wavelength of twice the depth of the heating, or 22 km, is predicted for large-scale heat sources, Holton et al. [2002] showed that smaller-scale heat sources will project more strongly on vertical wavelengths four times the depth of the heating. Our model simulations support the Holton et al. [2002] result, and show that such fast waves clearly appear in our simulations. In fact, they can dominate the convectively-generated gravity wave spectrum at wave periods shorter than a few hours.

6. Summary and Conclusions

We use satellite-based global precipitation and cloud data at high spatial and temporal resolution to estimate three-dimensional time-varying latent heating and the resulting global wave spectrum generated by convection. The modeled zonally-averaged gravity wave momentum fluxes in the lower stratosphere are similar to those derived from 3D satellite data, and similar to those observed by Pre-Concordiasi long-duration balloons. Modeled distributions of gravity wave momentum fluxes also display similar intermittency to the Pre-Concordiasi balloon measurements. These comparisons show that the modeled zonally-averaged fluxes fall within the range of variability seen in observations.

Interannual variations in gravity waves were examined in the context of interannual precipitation variations characterized by the ENSO 3.4 index. Spectra and intermittency of momentum flux were also evaluated. Profiles of momentum flux convergence were used to examine gravity wave forces acting on the QBO shear zones, and these forces were compared to planetary-scale tropical wave forces. The results show that in the zonal mean sense, the changes with ENSO are only modest, although regional variations in the gravity waves are large. For example, despite more rain and latent heating in the El Niño case, the zonal gravity wave momentum fluxes are smaller than in the La Niña case because of the shift in the precipitation to the central Pacific where upper tropospheric zonal winds are less favorable for vertical wave propagation. The more active MJO convection in the Indian Ocean/Maritime Continent region in the La Niña case appears to be a more important source in terms of gravity wave momentum fluxes.

The modeled intermittency in gravity wave amplitudes is similar to that observed in existing drifting isopycnal balloon measurements [Jewtoukoff et al. 2013], but current parameterization methods significantly underestimate this degree of intermittency in gravity waves above tropical convection, even with more realistic convective source parameterizations. Stochastic parameterization methods such as described in de la Cámara and Lott [2015] could be applied to the tropics utilizing these intermittency statistics, and we show evidence to suggest that such intermittency could improve the simulation of the QBO at lower levels where models show clear weaknesses, below $\sim$22 km (40 hPa). We further hypothesize that improving the simulation of the QBO at these lower altitudes might improve simulation of tropical-extratropical teleconnections and associated skill in long-range weather and seasonal climate forecasts.

In the future, we may have better observations to validate the inter-annual and regional variations in gravity wave momentum flux predicted in our model. Future measurements planned during the STRATEOLE-2 field campaign (www.strateole2.org) will provide a wealth of observations for model validation. Beginning in 2014, new precipitation measurements in the Global Precipitation Measurement (GPM) era have led to a new 30-min, $0.1^\circ \times 0.1^\circ$ resolution IMERG rain rate product [Huffmann et al., 2015]. These data are reportedly better constrained at higher frequencies, and may provide more accurate forcing for future model studies that can be more thoroughly validated with observations from STRATEOLE-2.

Acknowledgments. This work was supported by National Aeronautics and Space Administration's Aura Science Team program, with grant NNX14AE82G.

APPENDIX

Latent Heating

The latent heating algorithm we use to compute space-time gridded heating rates suitable for wave studies was described in Ryu et al. [2011]. There, they showed the zonal-mean heating profiles as functions of latitude in comparison to version 1 of the TRMM CSH latent heating product. Changes in version 2 of CSH resulted in stronger rates and a shift downward in the altitude of the peak heating. (See Tao et al. [2010]: their Fig. 10.) Considering these changes, our heating algorithm compared reasonably well in the mean to CSH. No high-frequency latent heating products exist for us to compare the higher-frequency variability. We instead validate our modeled gravity waves with observations in section 4.

A further examination of the heating input to the model is shown in Figure A1. These are average heating profiles over land and ocean regions within $\pm 30°$ latitude for Dec 2006 and Dec 2007. The heating profile shapes compare well to the TRMM SLH 15-yr means over land shown in Liu et al. [2015], although these ocean profiles display weaker secondary shallow heating than the 15-yr SLH means. The El Niño year (Dec 2006) shows less difference between heating over land and ocean than the La Niña year (Dec 2007), which is not surprising given the shifts in precipitation evident from Fig. 4. The active MJO during both of these months may be responsible for the higher peak heating magnitudes in these cases compared to multi-year means [Tao et al. 2010; Liu et al. 2015].

References

Alexander, M. J., 2015: Global and seasonal variations in three-dimensional gravity wave momentum flux from satellite limb-sounding temperatures. *Geophys. Res. Lett.*, **42 (16)**, 6860–6867, doi:10.1002/2015GL065234.

Alexander, M. J., and A. W. Grimsdell, 2013: Seasonal cycle of orographic gravity wave occurrence above small islands in the Southern Hemisphere: Implications for effects on the general circulation. *J. Geophys. Res.: Atmos.*, **118 (20)**, 11,589–11,599, doi:10.1002/2013JD020526.

Alexander, M. J., J. H. Richter, and B. R. Sutherland, 2006: Generation and trapping of gravity waves from convection, with comparison to parameterization. *J. Atmos. Sci.*, **63 (11)**, 2963–2977.

Andrews, D. G., J. R. Holton, and C. B. Leovy, 1987: *Middle Atmosphere Dynamics*. Academic Press, Orlando, 489 pp. pp.

Anstey, J. A., and T. G. Shepherd, 2014: High-latitude influence of the quasi-biennial oscillation. *Quar. J. Roy. Meteorol. Soc.*, **140 (678)**, 1–21, doi:10.1002/qj.2132.

Beres, J., 2004: Gravity wave generation by a 3-dimensional thermal forcing. *J. Atmos. Sci.*, **61**, 1805–1815.

Bergman, J. W., and M. L. Salby, 1994: Equatorial wave activity derived from fluctuations in observed convection. *J. Atmos. Sci.*, **51**, 3791–3806.

Bushell, A. C., N. Butchart, S. H. Derbyshire, D. R. Jackson, G. J. Shutts, S. B. Vosper, and S. Webster, 2015: Parameterized gravity wave momentum fluxes from sources related to convection and large-scale precipitation processes in a global atmosphere model. *J. Atmos. Sci.*, **72 (11)**, 4349–4371, doi:10.1175/JAS-D-15-0022.1.

Coy, L., K. Wargan, A. M. Molod, W. R. McCarty, and S. Pawson, 2016: Structure and dynamics of the quasi-biennial oscillation in MERRA-2. *J. Climate*, **29**, null, doi:10.1175/JCLI-D-15-0809.1.

de la Cámara, A., and F. Lott, 2015: A parameterization of gravity waves emitted by fronts and jets. *Geophys. Res. Lett.*, **42 (6)**, 2071–2078, doi:10.1002/2015GL063298.

de la Cámara, A., F. Lott, V. Jewtoukoff, R. Plougonven, and A. Hertzog, 2016: On the gravity wave forcing during the southern stratospheric final warming in LMDz. *J. Atmos. Sci.*, **73 (8)**, 3213–3226, doi:10.1175/JAS-D-15-0377.1.

dela Cámara, A., F. Lott, and A. Hertzog, 2014: Intermittency in a stochastic parameterization of nonorographic gravity waves. *J. Geophys. Res. Atmos.*, **119 (21)**, 11,905–11,919, doi:10.1002/2014JD022002.

Dunkerton, T., 1997: The role of gravity waves in the quasi-biennial oscillation. *J. Geophys. Res.*, **102**, 26,053–26,076.

Garfinkel, C. I., T. A. Shaw, D. L. Hartmann, and D. W. Waugh, 2012: Does the Holton-Tan mechanism explain how the quasi-biennial oscillation modulates the Arctic polar vortex? *J. Atmos. Sci.*, **69 (5)**, 1713–1733.

Geller, M. A., T. Zhou, and W. Yuan, 2016: The QBO, gravity waves forced by tropical convection, and ENSO. *J. Geophys. Res. Atmos.*, **121 (15)**, 8886–8895, doi:10.1002/2015JD024125.

Geller, M. A., and Coauthors, 2013: A comparison between gravity wave momentum fluxes in observations and climate models. *J. Climate*, **26**, 6383–6405.

Giorgetta, M. A., E. Manzini, and E. Roeckner, 2002: Forcing of the quasi-biennial oscillation from a broad spectrum of atmospheric waves. *Geophys. Res. Lett.*, **29 (8)**, 86–1 to 86–4.

Habib, E., A. T. Haile, Y. Tian, and R. J. Joyce, 2012: Evaluation of the high-resolution CMORPH satellite rainfall product using dense rain gauge observations and radar-based estimates. *J. Hydrometeorol.*, **13 (6)**, 1784–1798, doi:10.1175/JHM-D-12-017.1.

Hansen, F., K. Matthes, and L. J. Gray, 2013: Sensitivity of stratospheric dynamics and chemistry to QBO nudging width in the chemistry-climate model WACCM. *Journal of Geophysical Research: Atmospheres*, **118 (18)**, 10,464–10,474, doi:10.1002/jgrd.50812.

Held, I. M., and M. J. Suarez, 1994: A proposal for the intercomparison of the dynamical cores of atmospheric general circulation models. *Bull. Am. Meteorol. Soc.*, **75 (10)**, 1825–1830, doi:10.1175/1520-0477(1994)075⟨1825:APFTIO⟩2.0.CO;2.

Hertzog, A., M. J. Alexander, and R. Plougonven, 2012: On the intermittency of gravity-wave momentum flux in the stratosphere. *J. Atmos. Sci*, **69**, 3433–3448.

Hertzog, A., G. Boccara, R. A. Vincent, F. Vial, and P. Cocquerez, 2008: Estimation of gravity wave momentum flux and phase speeds from quasi-Lagrangian stratospheric balloon flights. Part II: Results from the VORCORE campaign in Antarctica. *J. Atmos. Sci.*, **65 (DOI: 10.1175/2008JAS2710.1)**, 3056–3070.

Holton, J., J. Beres, and X. Zhou, 2002: On the vertical scale of gravity waves excited by localized thermal forcing. *J. Atmos. Sci.*, **59**, 2019–2023.

Holton, J., and H.-C. Tan, 1980: The influence of the equatorial quasi-biennial oscillation on the global circulation at 50 mb. *J. Atmos. Sci.*, **37**, 2200–2208.

Holton, J. R., and W. M. Wehrbein, 1980: The role of forced planetary waves in the annual cycle of the zonal mean circulation of the middle atmosphere. *J. Atmos. Sci.*, **37 (9)**, 1968–1983, doi:10.1175/1520-0469(1980)037⟨1968:TROFPW⟩2.0.CO;2.

Huffman, G., D. T. Bolvin, D. Braithwaite, K. Hsu, R. Joyce, and P. Xie, 2015: NASA global precipitation measurement (GPM) integrated multi-satellite retrievals for GPM (IMERG). *Algorithm Theoretical Basis Document (ATBD)*, Version 4.5, NASA/GSFC, 30 pp.

Huffman, G. J., and Coauthors, 2007: The TRMM Multisatellite Precipitation Analysis (TMPA): Quasi-global, multiyear, combined-sensor precipitation estimates at fine scales. *J. Meteorol.*, **8**, 38–55.

Jewtoukoff, V., R. Plougonven, and A. Hertzog, 2013: Gravity waves generated by deep tropical convection: Estimates from balloon observations and mesoscale simulations. *J. Geophys. Res. Atmos.*, **118 (17)**, 9690–9707, doi:10.1002/jgrd.50781.

Joyce, R. J., J. E. Janowiak, P. A. Arkin, and P. Xie, 2004: CMORPH: A method that produces global precipitation estimates form passive microwave and infrared data at high spatial and temporal resolution. *J. Hydrometeorol.*, **5**, 487–503. [Data available online at http://www.cpc.ncep.noaa.gov/products/janowiak/cmorph_description.html]

Kawatani, Y., and K. Hamilton, 2013: Weakened stratospheric quasibiennial oscillation driven by increased tropical mean upwelling. *Nature*, **497**, 478–481.

Kawatani, Y., K. Sato, T. J. Dunkerton, S. Watanabe, S. Miyahara, and M. Takahashi, 2010b: The roles of equatorial trapped waves and three-dimensional propagating gravity waves in driving the quasi-biennial oscillation. Part II: Three-dimensional distribution of wave forcing. *J. Atmos. Sci.*, **67 (DOI:10.1175/2009JAS3223.1)**, 981–997.

Kawatani, Y., K. Sato, T. J. Dunkerton, S. Watanabe, S. Miyahara, and M. Takahashi, 2010a: The roles of equatorial trapped waves and three-dimensionally propagating gravity waves in driving the quasi-biennial oscillation. Part I: Zonal mean wave forcing. *J. Atmos. Sci.*, **67 (DOI:10.1175/2009JAS3222.1)**, 963–980.

Krismer, T. R., and M. A. Giorgetta, 2014: Wave forcing of the quasi-biennial oscillation in the Max Planck Institute Earth System Model. *J. Atmos. Sci.*, **71 (6)**, 1985–2006.

Liu, C., S. Shige, Y. N. Takayabu, and E. Zipser, 2015: Latent heating contribution from precipitation systems with different sizes, depths, and intensities in the tropics. *J. Climate*, **28 (1)**, 186–203.

Mote, P., and Coauthors, 1996: An atmospheric tape recorder: The imprint of tropical tropopause temperatures on stratospheric water vapor. *J. Geophys. Res.*, **101**, 3989–4006.

Newman, P. A., L. Coy, S. Pawson, and L. R. Lait, 2016: The anomalous change in the QBO in 20152016. *Geophys. Res. Lett.*, **43 (16)**, 8791–8797, doi:10.1002/2016GL070373.

Norton, W. A., 2006: Tropical wave driving of the annual cycle in tropical tropopause temperatures. Part II: Model results. *J. Atmos. Sci.*, **63 (May 2006)**, 1420–1431.

Ortland, D. A., M. J. Alexander, and A. W. Grimsdell, 2011: On the wave spectrum generated by latent heating. *J. Atmos. Sci.*, **68**, 2042–2060.

Osprey, S. M., N. Butchart, J. R. Knight, A. A. Scaife, K. Hamilton, J. A. Anstey, V. Schenzinger, and C. Zhang, 2016: An unexpected disruption of the atmospheric quasi-biennial oscillation. *Science*, **353 (6306)**, 1424–1427, doi:10.1126/science.aah4156.

O'Sullivan, D., and R. E. Young, 1992: Modeling the quasi-biennial oscillation's effect on the winter stratospheric circulation. *J. Atmos. Sci.*, **49 (24)**, 2437–2448, doi:10.1175/1520-0469(1992)049⟨2437:MTQBOE⟩2.0.CO;2.

Plougonven, R., A. Hertzog, and L. Guez, 2013: Gravity waves over Antartica and the Southern Ocean: Consistent momentum fluxes in mesoscale simulations and stratospheric balloon observations. *Q. J. Roy. Meteorol. Soc.*, **139**, 101–118.

Randel, W. J., F. Wu, S. J. Oltmans, K. Rosenlof, and G. E. Nedoluha, 2004: Interannual changes of stratospheric water vapor and correlations with tropical tropoapuse temperatures. *J. Atmos. Sci.*, **61**, 2133–2148.

Richter, J. H., A. Solomon, and J. T. Bacmeister, 2014: On the simulation of the quasi-biennial oscillation in the Community Atmosphere Model, version 5. *J. Geophys. Res. Atmos.*, **119**, 3045–3062, doi:10.1002/2013JD021122.

Rienecker, M. M., and et al., 2011: MERRA: NASA's Modern-Era Retrospective analysis for Research and Applications. *J. Climate*, **24**, 3624–3648. [Available online at https://gmao.gsfc.nasa.gov/reanalysis/MERRA/]

Ryu, J.-H., M. J. Alexander, and D. A. Ortland, 2011: Equatorial waves in the upper troposphere and lower stratosphere forced by latent heating estimated from TRMM rain rates. *J. Atmos. Sci.*, **68**, 2321–2342.

Salby, M. L., and R. Garcia, 1987: Transient response to localized episodic heating in the tropics. Part I: Excitation and short-time near-field behaviour. *J. Atmos. Sci.*, **44**, 458–498.

Sapiano, M. R. P., and P. A. Arkin, 2009: An intercomparison and validation of high-resolution satellite precipitation estimates with 3-hourly gauge data. *Journal of Hydrometeorology*, **10 (1)**, 149–166, doi:10.1175/2008JHM1052.1.

Sato, K., C. Tsuchiya, M. J. Alexander, and L. Hoffmann, 2016: Climatology and ENSO-related interannual variability of gravity waves in the Southern Hemisphere subtropical stratosphere revealed by high-resolution AIRS observations. *J. Geophys. Res. Atmos.*, **121 (13)**, 7622–7640, doi:10.1002/2015JD024462.

Scaife, A. A., and Coauthors, 2014b: Predictability of the quasi-biennial oscillation and its northern winter teleconnection on seasonal to decadal timescales. *Geophys. Res. Lett.*, **41 (5)**, 1752–1758, doi:10.1002/2013GL059160.

Scaife, A. A., and Coauthors, 2014a: Skillful long-range prediction of European and North American winters. *Geophysical Research Letters*, **41 (7)**, 2514–2519, doi:10.1002/2014GL059637, URL http://dx.doi.org/10.1002/2014GL059637.

Schirber, S., E. Manzini, T. Krismer, and M. Giorgetta, 2015: The quasi-biennial oscillation in a warmer climate: Sensitivity to different gravity wave parameterizations. *Climate Dynamics*, **45 (3-4)**, 825–836, doi:10.1007/s00382-014-2314-2, URL http://dx.doi.org/10.1007/s00382-014-2314-2.

Shige, S., Y. N. Takayabu, W.-K. Tao, and C.-L. Shie, 2007: Spectral retrieval of latent heating profiles from TRMM PR data. Part 2: Algorithm improvement and heating estimates over tropical ocean regions. *J. Appl. Meteorol. and Clim.*, **46**, 1098–1124.

Stephan, C., M. J. Alexander, and J. H. Richter, 2016: Characteristics of gravity waves from convection and implications for their parameterization in global circulation models. *Journal of the Atmospheric Sciences*, **73 (7)**, 2729–2742, doi:10.1175/JAS-D-15-0303.1.

Tao, W.-K., S. Lang, X. Zeng, S. Shige, and Y. Takayabu, 2010: Relating convective and stratiform rain to latent heating. *J. Climate*, **23**, 1874–1893.

Thompson, D. W. J., M. P. Baldwin, and J. M. Wallace, 2002: Stratospheric connection to Northern Hemisphere wintertime weather: Implications for prediction. *J. Climate*, **15**, 1421–1428.

TRMM Ancillary Data, 2016: Globally-merged Full Resolution IR Brightness Temperature Data. [Available online at https://disc.gsfc.nasa.gov/TRMM/data-holdings/data_access.html]

Tsuchiya, C., K. Sato, M. J. Alexander, and L. Hoffmann, 2016: MJO-related intraseasonal variation of gravity waves in the Southern Hemisphere tropical stratosphere revealed by high-resolution AIRS observations. *J. Geophys. Res. Atmos.*, **121 (13)**, 7641–7651, doi:10.1002/2015JD024463.

Ushio, T., and Coauthors, 2009: A Kalman filter approach to the global satellite mapping of precipitation (GSMAP) from combined passive microwave and infrared radiometric data. *J. Meteorol. Soc. Japan*, **87A**, 137–151.

Vadas, S. L., and H.-L. Liu, 2013: Numerical modeling of the large-scale neutral and plasma responses to the body forces created by the dissipation of gravity waves from 6 h of deep convection in Brazil. *Journal of Geophysical Research: Space Physics*, **118 (5)**, 2593–2617, doi:10.1002/jgra.50249.

Vadas, S. L., H.-L. Liu, and R. S. Lieberman, 2014: Numerical modeling of the global changes to the thermosphere and ionosphere from the dissipation of gravity waves from deep convection. *Journal of Geophysical Research: Space Physics*, **119 (9)**, 7762–7793, doi:10.1002/2014JA020280.

Wheeler, M. C., and H. H. Hendon, 2004: An all-season real-time multivariate MJO index: Development of an index for monitoring and prediction. *Mon. Wea. Rev.*, **132 (8)**, 1917–1932, doi:10.1175/1520-0493(2004)132⟨1917:AARMMI⟩2.0.CO;2.

Wright, C. J., S. M. Osprey, and J. C. Gille, 2013: Global observations of gravity wave intermittency and its impact on the observed momentum flux morphology. *J. Geophys. Res. Atmos.*, **118 (19)**, 10,980–10,993, doi:10.1002/jgrd.50869.

Yoo, C., and S.-W. Son, 2016: Modulation of the boreal wintertime Madden-Julian oscillation by the stratospheric quasi-biennial oscillation. *Geophys. Res. Lett.*, **43 (3)**, 1392–1398, doi: 10.1002/2016GL067762.

LIST OF TABLES

TABLE 1. Tropopause Momentum Flux Distribution Statistics

	Mean (mPa)	90^{th} Percentile	99^{th} Percentile
Dec 2006	9.5	19mPa/49%	46mPa/14%
Dec 2007	11	20mPa/54%	51mPa/18%

LIST OF FIGURES

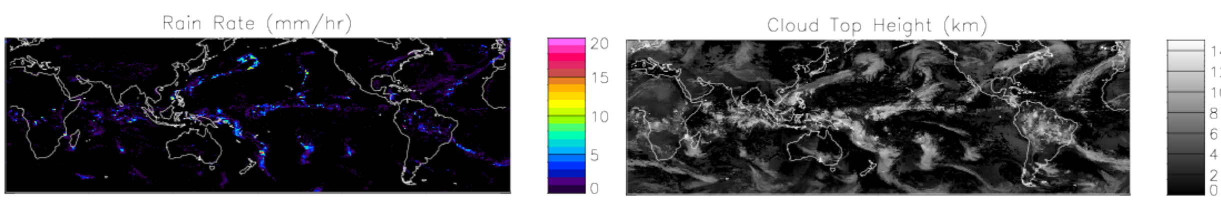

FIG. 1. Example snapshots of $0.25° \times 0.25°$ resolution rain rates (left) and cloud top heights (right) at 03:00 UT on 1 Dec 2006.

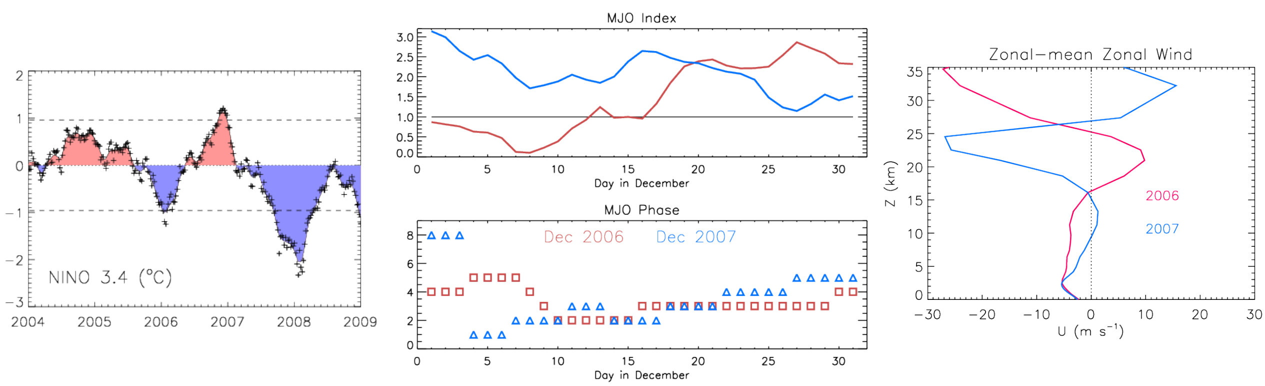

FIG. 2. Left: Time series of the monthly ENSO 3.4 sea surface temperature anomaly showing December 2006 and December 2007 as weak El Niño (>+1°) and moderate La Niña (<-1.5°) events, respectively. (Data source: NOAA/ESRL/PSD.) Center: MJO index (top) and phase (bottom) for Dec 2006 (red) and Dec 2007 (blue) as defined by the MJO Multivariate Index [Wheeler and Hendon, 2004]. Right: Wind profiles for Dec 2006 (red) and Dec 2007 (blue).

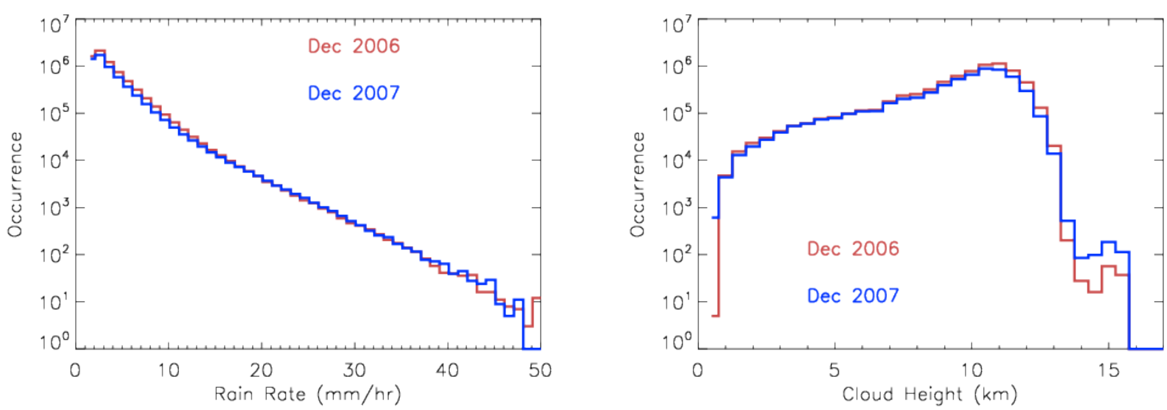

FIG. 3. Distributions of tropical 10°S-10°N rain rates (left) and cloud top heights (right) at $0.25° \times 0.25°$ resolution for "convective rain" points, those with rates exceeding 1.6 mm hr^{-1}. Colors indicate Dec 2006 (red) and Dec 2007 (blue).

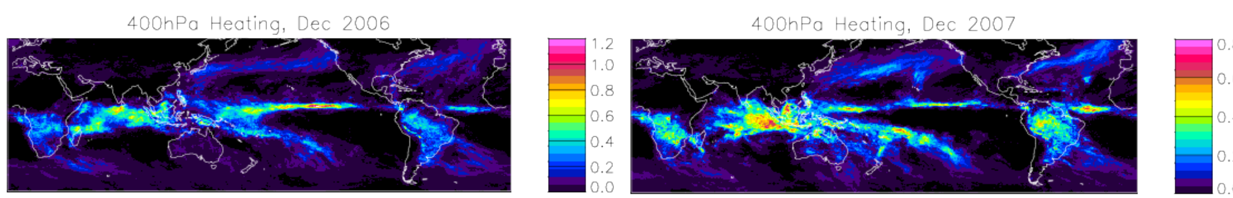

FIG. 4. Monthly-averaged 400 hPa latent heating (K hr^{-1}) mapped 60°S-60°N for December 2006 (left) and December 2007 (right) shown at $0.25° \times 0.25°$ resolution. The patterns illustrate typical ENSO variability.

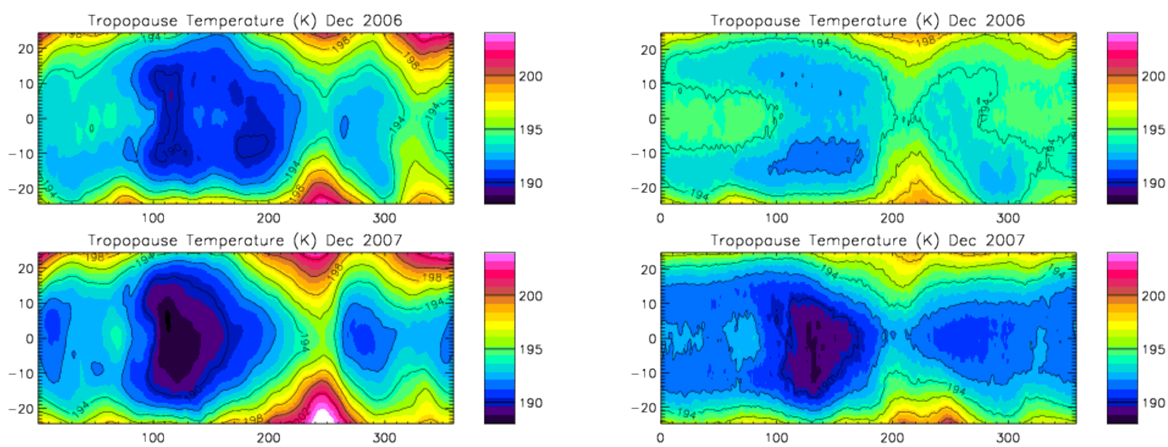

751 FIG. 5. Monthly-mean tropopause temperatures for Dec 2006 (top row) and Dec 2007 (bottom row). Left:
752 MERRA reanalysis. Right: Model.

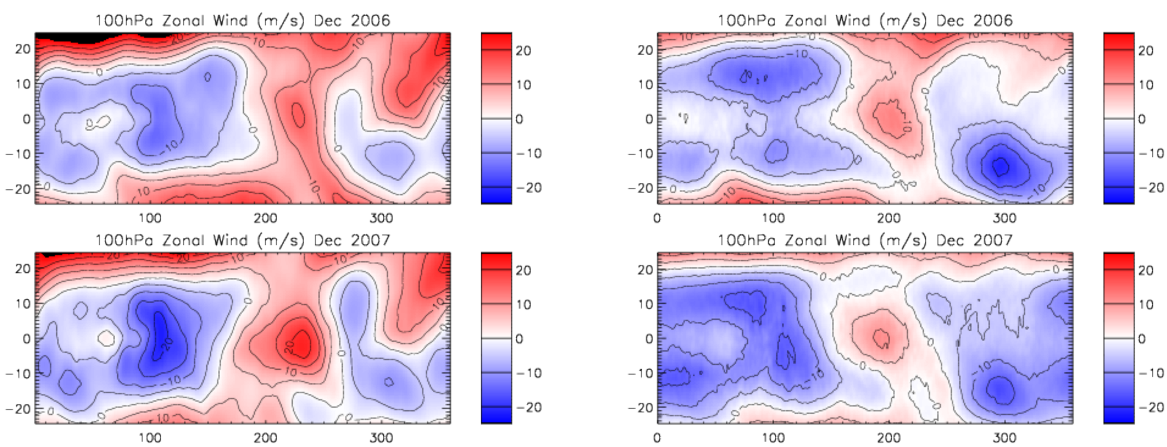

FIG. 6. Monthly-mean 100hPa zonal winds for Dec 2006 (top row) and Dec 2007 (bottom row). Left: MERRA reanalysis. Right: Model.

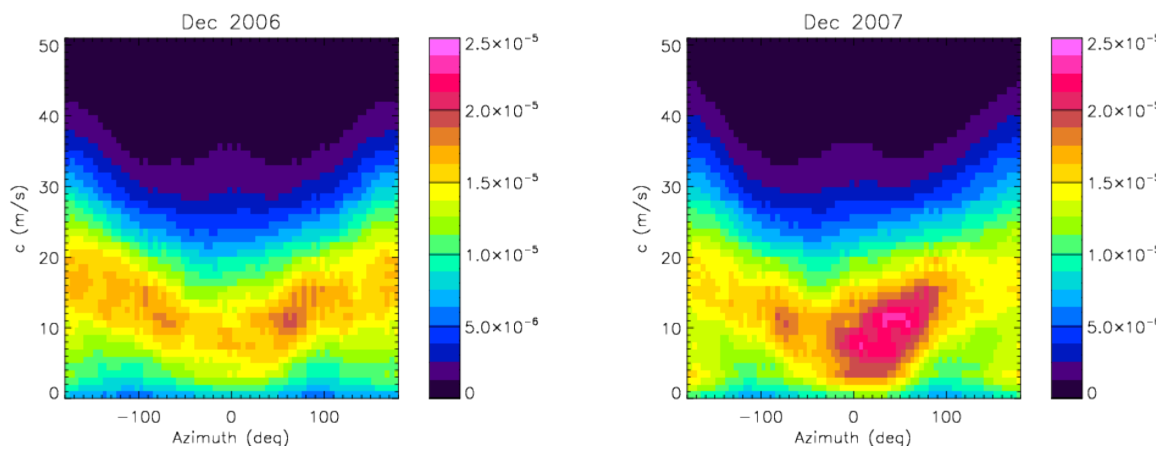

FIG. 7. Spectral density of gravity wave momentum flux at the tropopause in mPa deg^{-1} (m/s)$^{-1}$ as functions of azimuthal angle from east and phase speed for December 2006 (left) and December 2007 (right). The spectra are averaged between 15-17 km altitude.

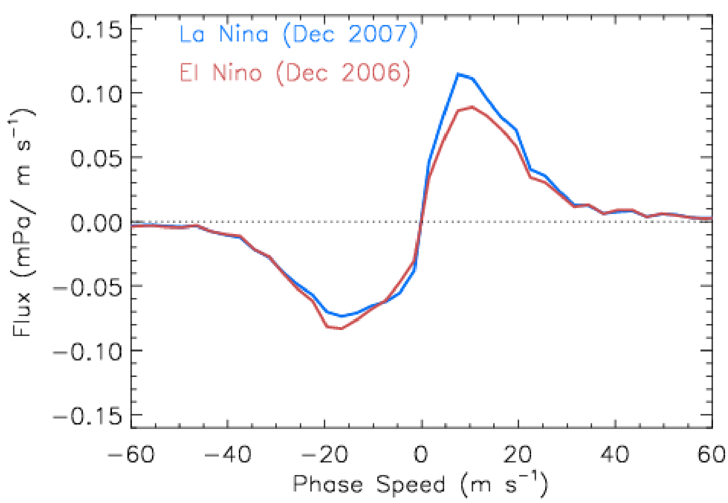

758 FIG. 8. Zonal gravity wave momentum fluxes (mPa/ms^{-1}) at the tropopause for Dec 2006 (red) and Dec 2007
759 (blue).

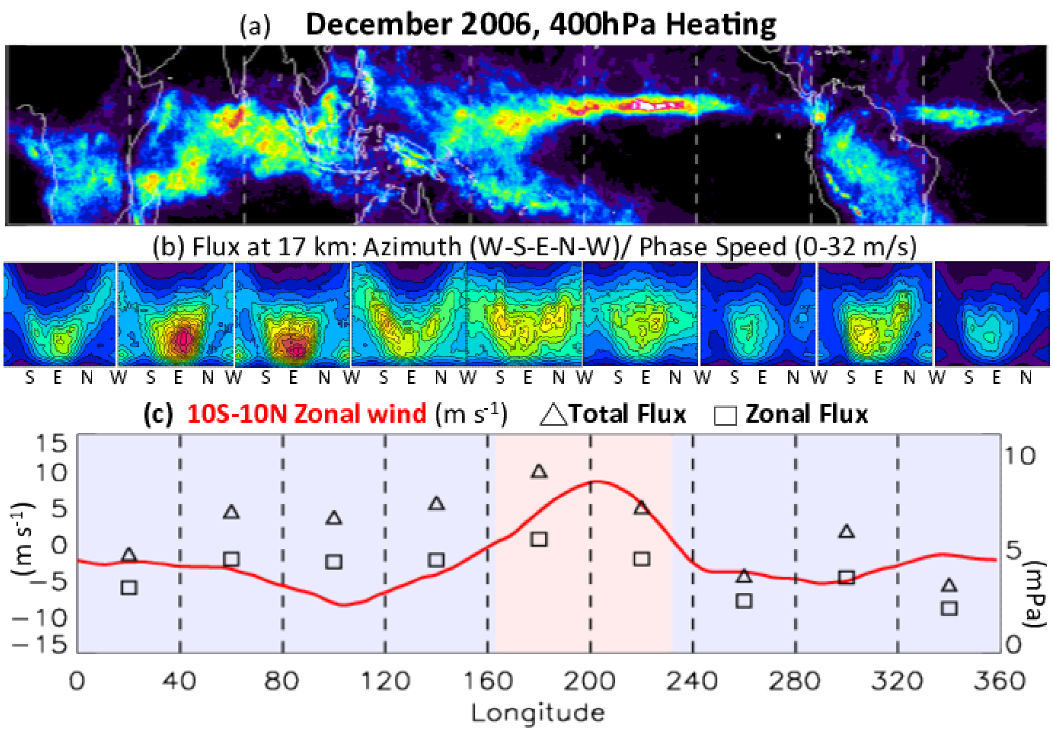

760 FIG. 9. Regional variations in the gravity wave momentum flux spectrum December 2006. (a) Map of the 400hPa latent heating (0-1 K hr^{-1}) shown for reference, with dashed lines marking each latitude/longitude sector. (b) Nine different azimuth (W-S-E-N-W) vs. phase speed (0-32 m s^{-1}) momentum flux spectra, one for each sector. (c) Equatorial 100hPa zonal wind (red, left axis) and momentum flux (symbols, right axis). Blue background marks westward winds, and pink marks eastward winds.

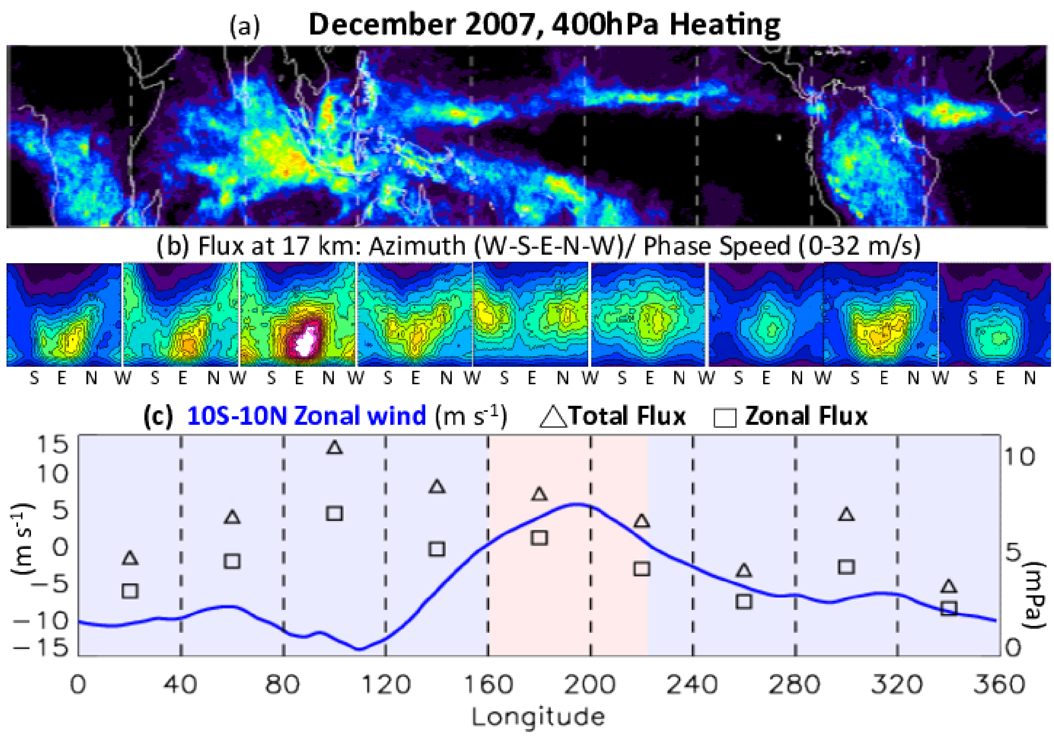

765 FIG. 10. Regional variations in the gravity wave momentum flux spectrum December 2007. (a) Map of the 400hPa latent heating (0-1 K hr^{-1}) shown for reference, with dashed lines marking each latitude/longitude sector. (b) Nine different azimuth (W-S-E-N-W) vs. phase speed (0-32 m s^{-1}) momentum flux spectra, below each sector. (c) Equatorial 100hPa zonal wind (blue, left axis) and momentum flux (symbols, right axis). Blue background marks westward winds, and pink marks eastward winds.

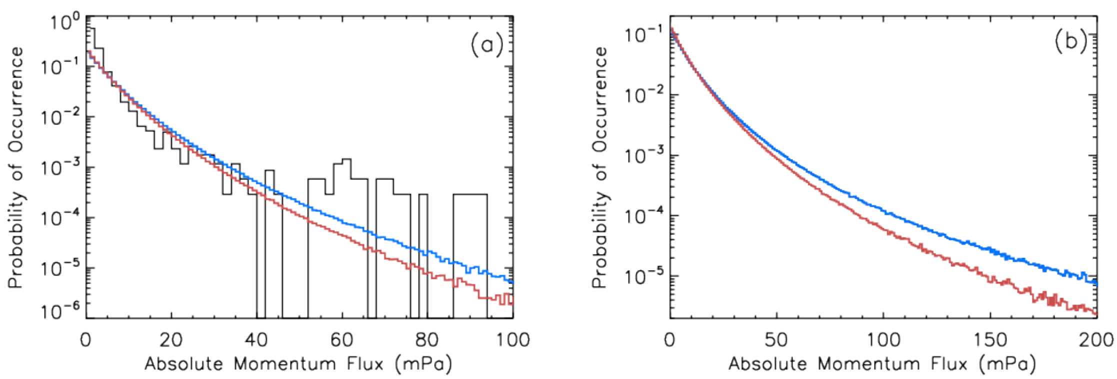

FIG. 11. Tropical (20S-20N) momentum flux distributions for Dec 2006 (red) and Dec 2007 (blue). (a) Distributions at 20 km. The black line shows the distribution derived from limb-sounding satellite observations (HIRDLS/COSMIC [Alexander 2015]) for Dec 2006-Dec 2007. (b) Distributions from the model at 17 km.

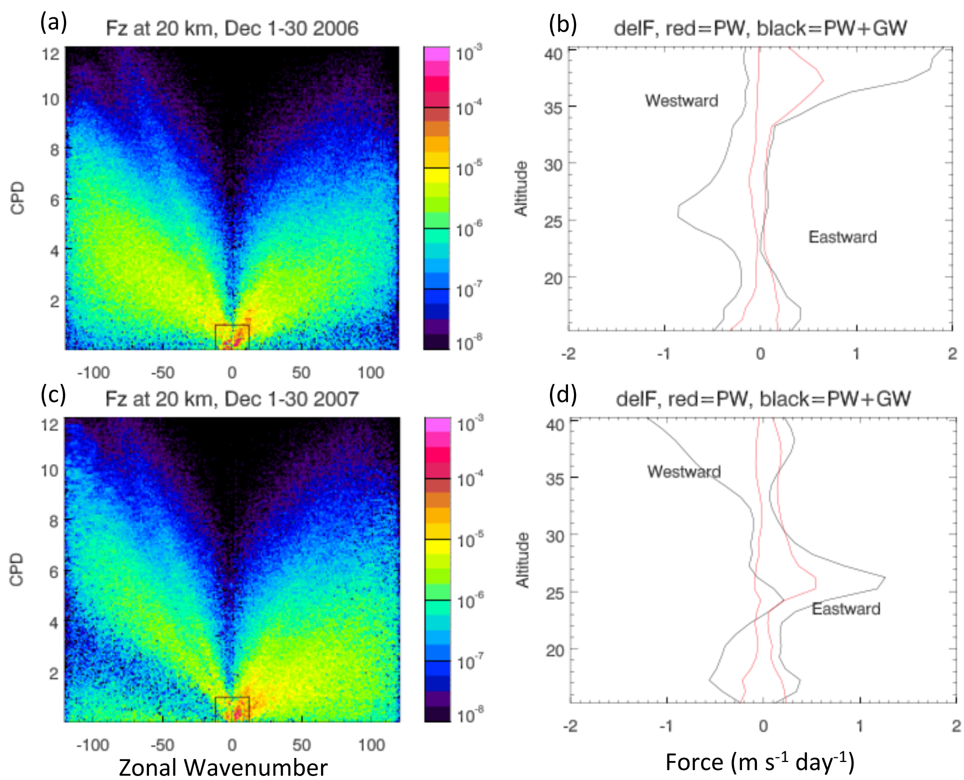

FIG. 12. (a) Dec 2006 zonal wavenumber-frequency spectrum of vertical Eliassen-Palm flux (F_Z) at 20 km with the small box near the origin indicating planetary-scale waves with frequencies <1 cyc d^{-1} and zonal wavenumbers <12. (b) Dec 2006 profiles of integrated F_Z divergence (force). Two black and two red profiles show spectra integrated separately over positive and negative wavenumbers, with positive and negative values respectively. Black profiles show the result from integrating the total spectrum while red show the integration only over the planetary-scale waves. (c) Same as (a) but for Dec 2007. (d) Same as (b) but for Dec 2007.

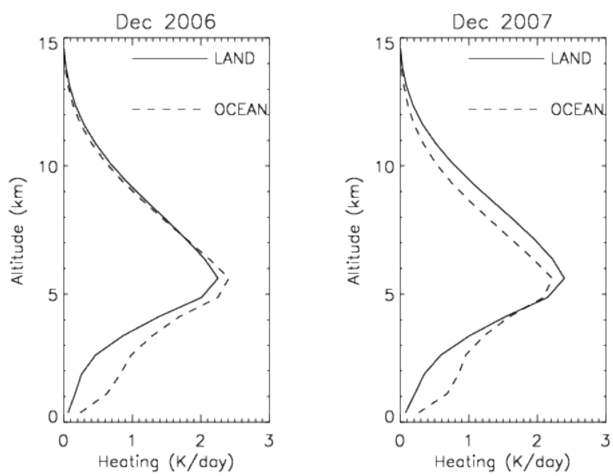

779 Fig. A1. Profiles of latent heating averaged over land (solid) and ocean (dashed). Left: December 2006.
780 Right: December 2007.